Tailoring Staircase-like Hysteresis Loops in Electrodeposited Tri-segmented Magnetic Nanowires: a Strategy towards Minimization of Interwire Interactions

Jin Zhang[†], Sebastià Agramunt-Puig[†], Núria Del-Valle[†], Carles Navau[†], Maria D. Baró[†], Sònia Estradé[‡], Francesca Peiró[‡], Salvador Pané[§], Bradley Nelson[§], Alvaro Sanchez[†], Josep Nogués[#,§], Eva Pellicer[†,], and Jordi Sort[†,§,*]*

[†]Departament de Física, Universitat Autònoma de Barcelona, E-08193 Bellaterra, Barcelona, Catalonia, Spain

[‡]LENS, MIND-IN2UB, Departament d'Electrònica, Universitat de Barcelona, Martí i Franquès 1, E-08028 Barcelona, Spain

[§]Institute of Robotics & Intelligent Systems (IRIS), ETH Zürich, CH-8092 Zurich, Switzerland

[#]Catalan Institute of Nanoscience and Nanotechnology (ICN2), CSIC and The Barcelona Institute of Science and Technology, Campus UAB, Bellaterra, 08193 Barcelona, Spain

[§]Institució Catalana de Recerca i Estudis Avaçats (ICREA), Barcelona, Catalonia, Spain

KEYWORDS: segmented nanowires, magnetic interactions, template-assisted electrodeposition, staircase hysteresis loops, nanomagnetism

1

ABSTRACT A new strategy to minimize magnetic interactions between nanowires (NWs) dispersed in a fluid is proposed. Such strategy consists in preparing tri-segmented NWs containing two antiparallel ferromagnetic segments with dissimilar coercivity separated by a non-magnetic spacer. The tri-segmented NWs exhibit a staircase-like hysteresis loop with tunable shape that depends on the relative length of the soft- and hard-magnetic segments and the respective values of saturation magnetization. Such NWs are prepared by electrodepositing CoPt/Cu/Ni in a polycarbonate (PC) membrane. The antiparallel alignment is set by applying suitable magnetic fields while the NWs are still embedded in the PC membrane. Analytic calculations are used to demonstrate that the interaction magnetic energy from fully-compensated tri-segmented NWs with antiparallel alignment is reduced compared to a single-component NW with the same length or the tri-segmented NWs with the two ferromagnetic counterparts parallel to each other. The proposed approach is appealing for the use of magnetic NWs in certain biological or catalytic applications where the aggregation of NWs is detrimental for optimized performance.

1. Introduction

Owing to their unique physicochemical properties, materials structured in the form of one-dimensional nanoarchitectures, such as nanorods and nanowires (NWs), have found widespread applications in several technological areas, e.g. optoelectronics,[1] magnetism,[2,3] catalysis,[4] piezo- and thermo-electricity,[5,6] biosensing,[7,8] and micro-/nanoelectromechanical systems (MEMS/NEMS),[9] among others. Specifically, ferromagnetic NWs are being employed as components in information storage and logic devices,[3,10,11] spintronics,[12] magnetic sensors,[13] and also as platforms in the biomedical field (e.g., hyperthermia or drug delivery).[14]

To further expand their range of applications, the implementation of other materials with dissimilar nature within the NW architecture can provide additional and complementary functionalities. The resulting hybrid structures (i.e., core-shell NWs or segmented NWs) offer enhanced performance either due to the established synergy between the properties of each building block, or due to interfacial interaction effects between them. Segmented NWs can be all-electrodeposited in a cost-effective manner,[15-18] while core-shell NW structures usually require the combination of different synthetic approaches (e.g., electrodeposition together with chemical vapor deposition).[19] In the field of magnetism, segmented NWs served as a model system for heterostructured junctions that exhibit various fascinating perpendicular spin transport phenomena, such as current-perpendicular-to-plane giant magnetoresistance (GMR)[20,21] or tunneling magnetoresistance (MR)[22], to name a few. Likewise, core/shell NWs[23] combining several phases of distinct magnetic properties could generate additional effects—spintronic, multiferroic, magnetoplasmonic, etc. These outstanding properties have furnished hybrid NWs a host of applications in giant magnetoresistance sensors,[24] spring-magnets,[25] exchange bias systems,[26] nanomagnet microwave resonators[27] or magneto-plasmonics devices.[28]

Once released from the template or detached from the substrate, self-standing magnetic NWs can be dispersed in fluids and subsequently manipulated using external magnetic fields and field gradients. Wireless magnetic actuation is crucial for the utilization of these NWs in certain biological or catalytic applications.[18,19,29-31] However, one of the most challenging issues in areas like drug delivery or biological labeling is to avoid the aggregation of NWs once the external magnetic field is removed. Agglomeration of NWs inside bodily fluids can cause obstruction of the vessels, eventually leading to thrombosis or even more serious health diseases.

The formation of NWs bundles is also a serious concern in applications that require the use of a single NW, for example when a single NW is intended to be bound to cells or proteins[32] or in NWs that need to be precisely attached to small components to build sophisticated miniaturized devices.[33] Also, aggregation of NWs has to be prevented in order to obtain high-quality homogeneous ferrofluids or to preserve the mechanical properties of composites containing magnetic NWs.[13]

Magnetic dipolar interactions between magnetic particles dispersed in liquids are directly responsible for their agglomeration. In the absence of a magnetic field, such interactions are proportional to the overall remanent magnetization of each particle. For this reason, superparamagnetic nanoparticles, with zero net remanent magnetization, are usually preferred in comparison to NWs for certain biological applications.[31] Nevertheless, their exceedingly small surface area limits their efficiency as drug carriers. An alternative approach is to use magnetic vortices,[34] also with virtually zero magnetic remanence, but disks of a few micrometers in diameter are needed to form such magnetic configurations. Hence, magnetic vortices can be rather impractical for most biological purposes.

Ferromagnetic NWs offer some advantages with respect to superparamagnetic nanoparticles or microstructured disks exhibiting magnetic vortices. However, a smart strategy to tailor (and, in particular, to reduce) the overall remanent magnetization of magnetic NWs is needed in order to control (and decrease) the strength of interwire dipolar interactions to minimize aggregation. It is well-known that some of the properties of magnetic NWs (e.g., the effective magnetic anisotropy direction or the coercivity) are strongly dependent on the diameter and aspect ratio as well as on the dipolar coupling between the ferromagnetic segments.[35] For example, Liu and coworkers[36] have electrodeposited Co/Cu multilayered NWs, in which the magnetic configurations can be tuned by adjusting the Co segment aspect ratio. In turn, the saturation magnetization depends mainly on the composition of the NWs.

In this work, the possibility to tune the remanent magnetization of NWs is demonstrated by synthesizing tri-segmented NWs in which the orientation of the different segments comprising the NWs is individually controlled, similarly to what has been successfully demonstrated in synthetic ferrimagnets,[37] patterned multilayers for multi-bit data storage[38] or recently proposed in core/shell nanoparticles.[39,40] To this end, arrays of tri-segmented CoPt/Cu/Ni NWs (i.e., hard- and soft-ferromagnetic segments separated by a non-magnetic Cu spacer) embedded in polycarbonate (PC) membranes have been prepared by electrodeposition. Magnetic measurements of the hybrid NWs, while still embedded in the PC templates, reveal the occurrence of staircase-like hysteresis loops, resulting from the two different coercivities of the soft and hard ferromagnetic segments. The overall shape of the hysteresis loops (i.e., the magnetization step sizes) can be tuned by varying the aspect ratio of the different segments. Antiparallel alignment between the CoPt and Ni segments can be established after saturation by applying a negative magnetic field larger than the coercivity exhibited by Ni but lower than the

coercivity corresponding to CoPt. In such antiparallel alignment, proper adjustment of the Ni and CoPt segment length leads to either positive or negative remanent magnetization, eventually even resulting in zero remanent net magnetization (fully compensated NWs). The tri-segmented NWs can be easily released from the PC membrane and satisfactorily dispersed in fluids. Analytical calculations are used to corroborate that the interaction magnetic energy between two fully-compensated tri-segmented NWs (with two antiparallel magnetic segments) is generally reduced with respect to a tri-segmented NW having the two segments parallel to each other.

2. Experimental section

2.1. Synthesis of the tri-segmented NWs

Template-assisted electrodeposition was carried out in a typical single-compartment double-jacketed glass electrochemical cell. Track-etched PC membranes with 30 nm nominal pore size (Nuclepore, Whatman) were used as working electrodes (WE). PC membranes with well-separated pores were selected for two reasons: (i) these membranes can afford the basic pH values needed to grow CoPt, (ii) the distance between neighboring NWs is sufficiently high to ensure that interwire dipolar magnetic interactions between NWs are negligible, so that their behavior when still embedded in the PC membrane is essentially the same as that of an isolated non-interacting NW. The fabrication process of tri-segmented NWs is illustrated in Scheme 1.
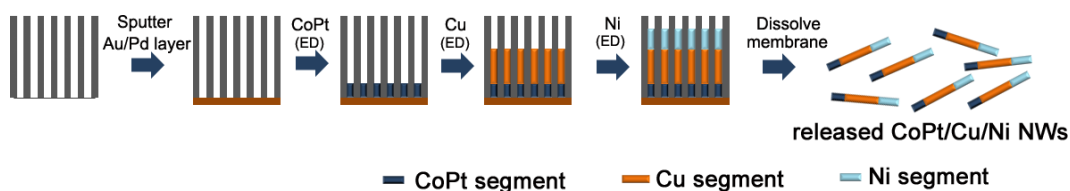
Scheme 1. Schematic picture of tri-segmented NWs fabrication process using PC template-based electrodeposition. "ED" stands for electrodeposition.

First, a thin Au-Pd layer was sputtered onto one side of PCs to make them conductive. The Au-Pd surface was put in contact with a copper plate, held inside a plastic stationary holder, and a circular area of 3.14 cm^2 was exposed to the electrolyte for deposition. Before electrodeposition, the PC membrane was placed in an ultrasonicator for 3 min in order to remove the air inside the PC channels. In this way, the electroactive species can penetrate inside the channels and access the Au-Pd layer, thereby enabling the electrodeposition. A platinum wire was utilized as counter electrode, which was positioned vertically facing the WE. A double junction Ag|AgCl 3M KCl electrode ($E = + 0.210$ V versus standard hydrogen electrode) was used as reference electrode to record the potential at the WE. The three electrodes were connected to a PGSTAT302N Autolab potentiostat/galvanostat (Ecochemie).

The tri-segmented NWs were prepared via sequential direct current electrodeposition of CoPt, Cu and Ni segments by changing the corresponding electrolytes. The deposition of the CoPt segments was performed galvanostatically at $j = -10$ mA cm^{-2}, pH = 8.5, T = 65°C. The electrolyte consisted of 30 mM Co(SO$_3$NH$_2$)$_2$·xH$_2$O, 2 mM Pt(NH$_3$)$_2$(NO$_2$)$_2$, 0.1 M glycine, 0.1 M sulfamic acid, 5 mM saccharine, and 0.1 M sodium citrate. The electrodeposition of Cu segments was carried out potentiostatically at $E = -1.0$ V in an electrolyte containing 0.2 M CuSO$_4$·5H$_2$O and 0.1 M boric acid. The third segment (Ni) was grown galvanostatically at $j = -10$ mA cm^{-2} from an electrolyte consisting of 2 M NH$_4$Cl and 0.1 M NiCl$_2$. The deposition processes for Cu and Ni segments were carried out at 25°C and the pH was left unadjusted (i.e., preparation pH). All the electrolytes were de-aerated before and during the experiments in order

to get rid of dissolved oxygen and to ensure the homogeneity of the solution. For electron microscopy observations, the tri-segmented NWs were released by dissolving the PC template in chloroform and washed several times afterwards. For the sake of comparison, single-component Ni, Cu and CoPt NWs were also electrodeposited using the same conditions as for the hybrid NWs.

2.2. Structural characterization

Scanning electron microscopy (SEM) images and energy-dispersive X-ray spectroscopy (EDX) compositional analyses were acquired using a Merlin Zeiss microscope operated at 3 kV and 15 kV, respectively. Specimens for SEM and EDX measurements were prepared via drop-casting a droplet of NWs suspended in chloroform onto an aluminum foil and subsequent drying in air. Similar preparation method onto Cu grids was used for TEM observations. The structure and morphology of the NWs (length of the different segments, aspect ratio, etc.) were also investigated by high-resolution transmission electron microscopy (HRTEM) using a Jeol-JEM 2011 system with a field emission gun operating at 200 kV. Electron energy loss spectra (EELS) were acquired along the NWs. Spectra were taken in the 650-1150 eV energy loss range, where the Co L2,3, the Cu L2,3 and the Ni L2,3 edges were found, at 779 eV, 931 eV and 855 eV, respectively. The quantitative analysis of the EELS spectra was performed using the homemade software package Oxide Wizard.[41] X-ray diffraction (XRD) patterns of the NWs were recorded on a Philips X'Pert diffractometer in the 30-100° 2θ range (step size = 0.026°, step time = 2000

s) using Cu K_{α} radiation ($\lambda = 0.154178$ nm). In this case, the PC membrane was not dissolved – the XRD patterns were acquired while the NWs were still embedded inside the membrane.

2.3. Magnetic characterization

Hysteresis loops were collected on the single-component (CoPt and Ni) and tri-segmented (CoPt/Cu/Ni) NWs at room temperature using a vibrating sample magnetometer (VSM) from Oxford Instruments, with a maximum applied magnetic field of 0.5 Tesla. An antiparallel alignment between the CoPt and Ni segments was settled by first saturating the NWs in the positive direction and then applying a negative magnetic field sufficient to reverse Ni but lower than the coercivity of the CoPt segment.

3. Results and discussion

3.1. Structure and magnetic behavior of single-component CoPt and Ni

All the investigated NWs were deposited inside the channels (i.e., pores) of PC membranes that are visible as black spots by SEM imaging (see Figure S1 in the Electronic Supplementary Information). These pores traverse the membranes completely, hence allowing the growth of the NWs by electrodeposition. The thickness of the PC membranes is approximately 5 μm, the average pore diameter (at the surface of the PC template) ranges from 40 to 60 nm and there is an areal density of less than 10 pores μm^{-2}. Single-component NWs consisting of CoPt alloy, Cu and Ni were first deposited individually, in order to estimate and optimize the growth rates.
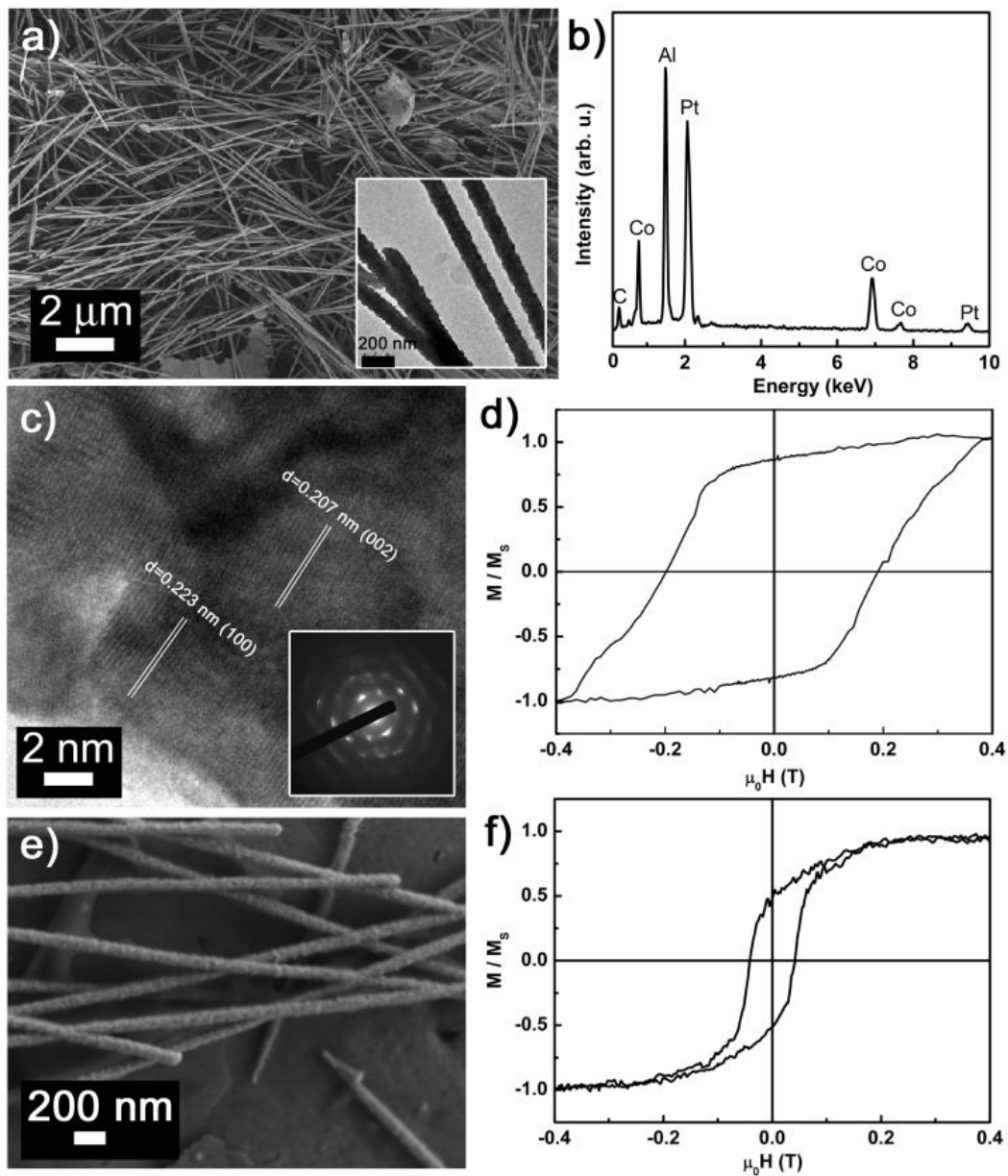
Figure 1. a) SEM, b) EDX spectrum and c) HRTEM image of CoPt NWs released from the PC membrane, d) room-temperature magnetic hysteresis loop of single-component CoPt NWs arrays (measured before PC removal, along the NWs axis), e) SEM image of single-component Ni NWs released from the PC membrane, and f) room temperature hysteresis loop of single-component Ni NWs arrays (embedded in the PC membrane). Insert in a) shows a magnified view of a few CoPt NWs, whereas insert in c) shows a SAED pattern of CoPt NWs.

As shown in Figure 1a, CoPt NWs can be obtained in high-yields, with a length of around 5 μm and a diameter about 100 nm (see also the corresponding TEM image, as inset of Figure 1a). The larger diameter of the NWs, as compared to the average pore diameter at the surface of the PC membranes, indicates that the channels inside the PC are probably not completely homogeneous in width. This is actually supported by previous works from the literature in which it has been suggested that the pores inside PC templates are not completely cylindrical (with a constant cross-section) but, instead, appear to be "cigar-like shaped"[42]. The NWs have all similar lengths, suggesting that their growth proceeds at the same rate over the whole PC area. This is an important feature for the subsequent fabrication of the tri-segmented NWs. The EDX spectrum (Figure 1b) confirms that the NWs are composed of Pt and Co, with a mean atomic composition $Co_{70}Pt_{30}$. The aluminum signal in Figure 1b comes from the aluminum foil onto which the NWs were drop-casted. The HRTEM and the associated SAED pattern (Figure 1c and inset) reveal that the CoPt NWs are polycrystalline (hexagonal closed-packed, hcp, phase) with clear lattice fringes. The obtained interplanar distances can be ascribed to the (100) and (002) planes of hcp structure. Representative SEM images of the Ni and Cu single-component NWs are shown in Figures 1e and S2 (see Electronic Supplementary Information), respectively. Similar to CoPt NWs, well-grown, continuous Cu and Ni NWs can be deposited with an approximate diameter of 100 nm.

Typical XRD patterns of the as-deposited CoPt, Cu and Ni NWs embedded in the PC membrane are shown in Figure 2. For both Cu and Ni single-component NWs, the (111), (200), (220) and (311) reflections of face-centered cubic (fcc) structure are detected. In addition, for Cu NWs, by comparing the tabulated and experimental relative peak intensities (*I*) of the (111) and (200) reflections, clear conclusions about crystallographic texture can be drawn.
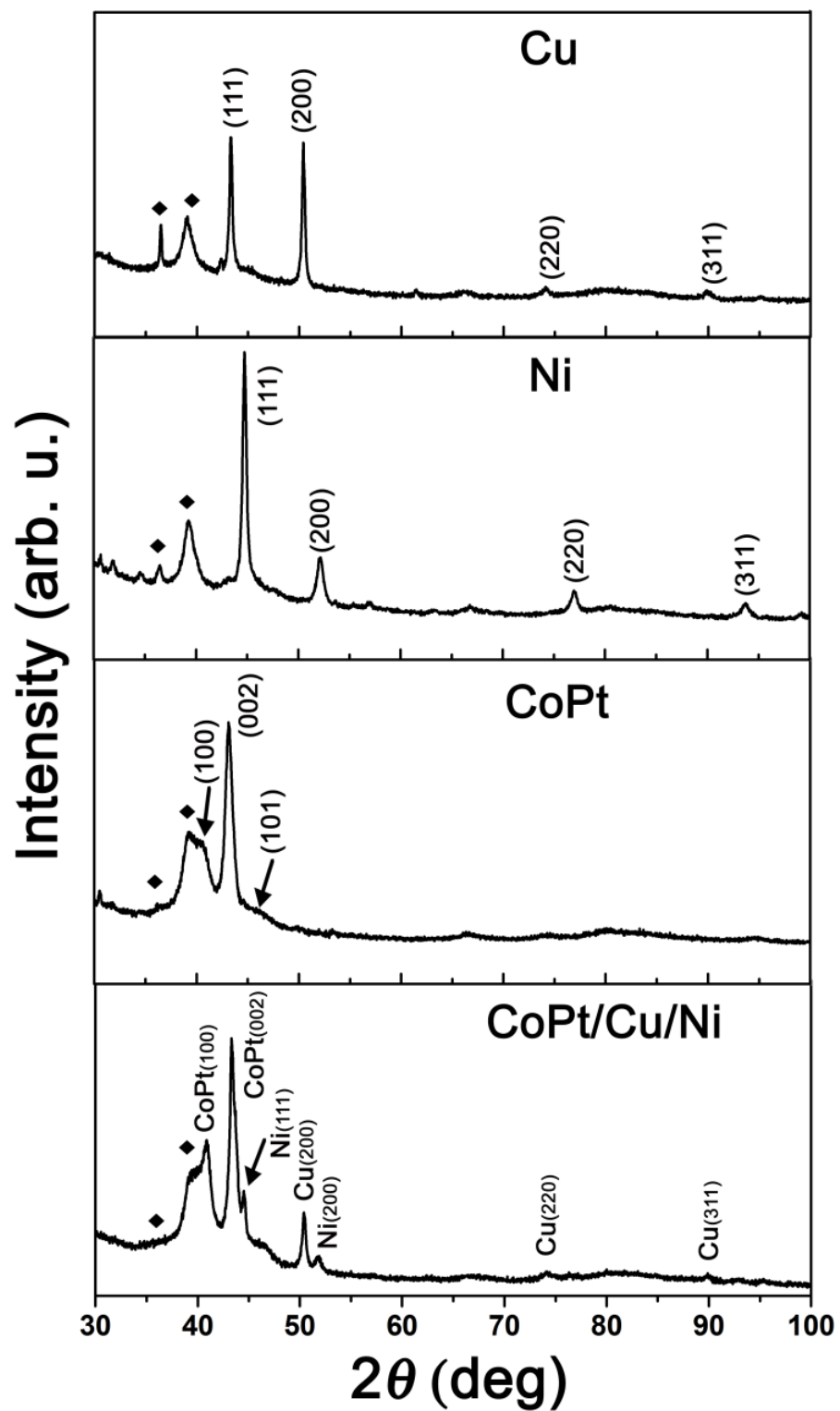
Figure 2. XRD patterns of single-component Cu, Ni and CoPt NWs and tri-segmented CoPt/Cu/Ni NWs. Peaks denoted by ♦ belong to the sputtered Au-Pd conductive layer.

Namely, the experimental I_{200} / I_{111} ratio is 1.02, which is larger than the theoretical value (0.46) for randomly oriented Cu grains. This indicates the formation of [100] textured Cu NWs. Textures in electrodeposited materials are highly influenced by electrolyte composition and working conditions. Thus, either non-textured or textured materials can be readily obtained by simply changing the plating parameters.

The diffractogram of single-component CoPt NWs reveals that the strongest peak appears at $2\theta = 43.13°$. This position matches both hcp and fcc phases. However, the absence of any reflection at ca. 51.5° suggests that CoPt has crystallized in the hcp structure, as it corresponds to Co-rich NWs electrodeposited in basic pH conditions.[43] The intensity of the (101) reflection is dramatically reduced as compared to the standard powder pattern, which suggests that the hexagonal c axis lies preferentially along the long axis of the NWs.

The magnetic hysteresis loop of the single-component CoPt NW arrays measured with the applied field parallel ($H_{//}$) to the long axis of the NWs is shown in Figure 1d. The coercivity, H_C, is about 1950 Oe. Therefore, CoPt NWs show hard-ferromagnetic behavior. The magnetic properties of single-component Ni NWs were measured under the same conditions as for CoPt NWs. As shown in Figure 1f, H_C is around 410 Oe in this case. According to these data, it is clear that hard magnetic/spacer/soft magnetic tri-segmented CoPt/Cu/Ni NWs could be, in principle, successfully deposited into PC membranes by simply changing the electrolyte.

3.2. Structural characterization of tri-segmented NWs

The XRD pattern of the as-deposited tri-segmented CoPt/Cu/Ni NW arrays embedded in the PC membrane is shown at the bottom of Figure 2. By comparing the XRD patterns of single-

component and tri-segmented CoPt/Cu/Ni NWs all the peaks corresponding to CoPt, Cu and Ni phases can be straightforwardly indexed. Hence, the sequential fabrication process did not brought any extra phases or impurities. Therefore, CoPt/Cu/Ni tri-segmented NWs can be successfully synthesized through a template-based electrodeposition method.
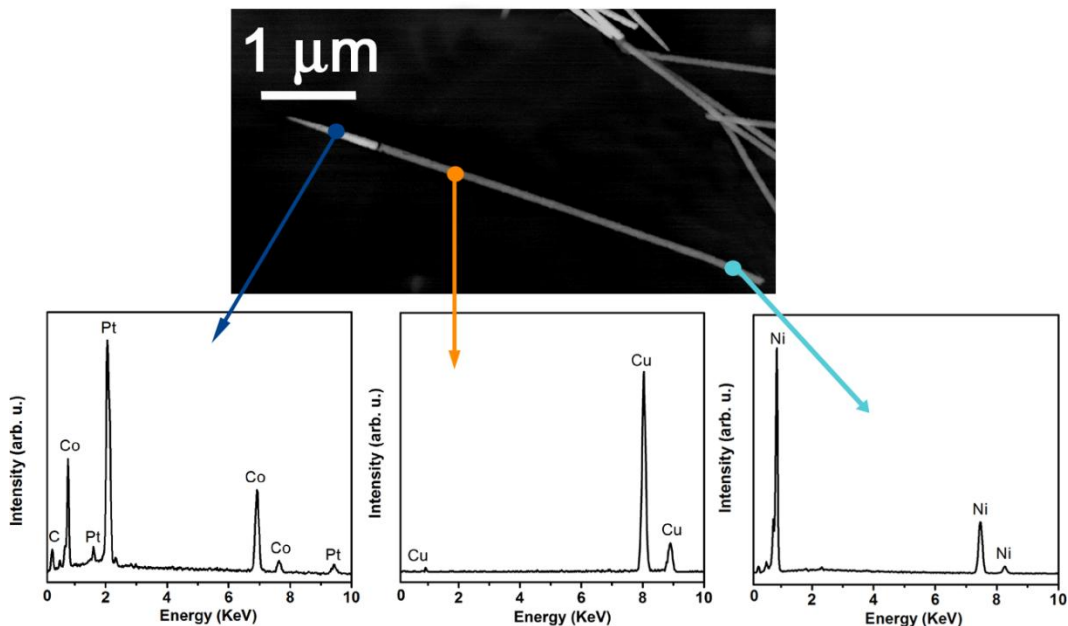

Figure 3. EDX spectra acquired in each of the segments of the tri-segmented NW shown in the upper TEM image. Note that no clear interface between Cu and Ni can be seen using standard TEM conditions.

The compositional variations along the NW axis were assessed by EDX (see Figure 3). A TEM image of a whole tri-segmented NW can be observed in the upper panel of Figure 3. NWs show a sharp needle-like end due to the narrowing of the PC pores near the surface, in agreement with the literature.[42] The darker and brighter contrast reveals the difference in atomic weight between the constituent phases, being the electron dispersing capability of CoPt stronger than for both Cu

and Ni. Since Cu and Ni have similar atomic weight, it is difficult to clearly distinguish them by TEM. Therefore, the brightest region stands for CoPt while the darker regions represent the Cu + Ni segments.
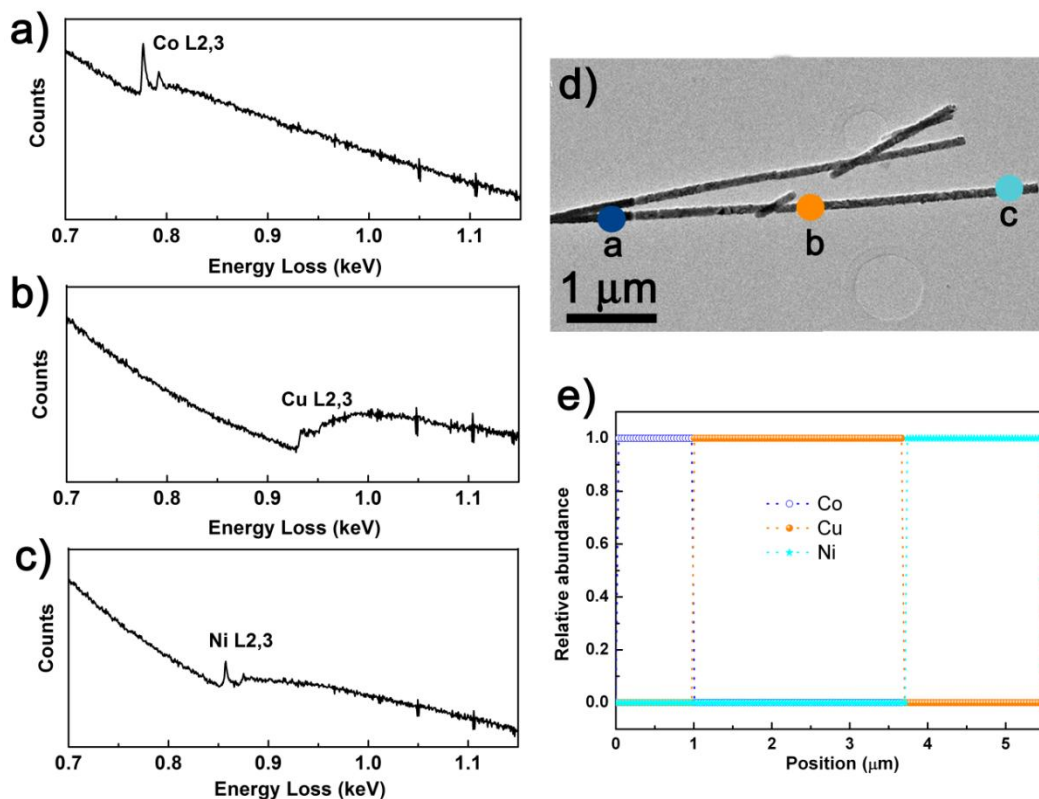

Figure 4. a-c) EELS point spectra for CoPt/Cu/Ni tri-segmented NWs [marked as a, b and c in (d)]. d) STEM image of CoPt/Cu/Ni tri-segmented NW for which an EELS line-scan was performed. The corresponding element distribution as a function of NW length is shown in e).

To gain further insight into the heterostructured architecture of the NWs, STEM-EELS analyses were performed (Figure 4). EELS analyses were actually necessary to distinguish between the Cu and Ni segments and, in turn, to determine their lengths. When the electron beam

was spotting in "a", Co was detected (Figure 4a). When the electron beam was directed to the middle part of the NW (point "b"), only Cu was visible (Figure 4b). Similarly, the EELS analysis on point "c" (Figure 4c) clearly confirms that the ending segment of the NW is made of pure Ni. EELS line-scan was used to determine the length of the different segments, as shown in Figures 4d and 4e. In this particular case (referred to as "sample D" in Section 3.3), the length of the CoPt segment, which now corresponds to the darker region, is 0.97 μm, whereas the Ni segment has a length of 1.74 μm. Finally, the Cu segment, with a length of 2.72 μm, is sandwiched between CoPt and Ni. In turn, EELS analysis performed in the NWs with shorter Ni segments (sample A in section 3.3) reveals that the CoPt, Cu and Ni segment lengths are 1.10, 2.63 and 0.61 μm, respectively.

3.3. Magnetic characterization of the tri-segmented NWs

Hysteresis loops from various arrays of CoPt/Cu/Ni tri- segmented NWs embedded in the PC membrane, measured along the NWs axis, are shown in Figure 5. The loops exhibit a staircase-like shape with two well-differentiated coercivities, corresponding to the magnetization reversal of Ni (soft segment) and CoPt (hard segment), respectively. These two switching events can be clearly seen since (i) the magnetic dipolar interactions between neighboring NWs in the PC membranes are small (due to the large interpore distance), and (ii) the segments in each nanowire are separated by the non-magnetic Cu spacer to avoid magnetic exchange interactions between CoPt and Ni. Otherwise, if the NWs were deposited close to each other (as in conventional anodized aluminum oxide templates), the loops would become tilted and the staircase shape would be lost.[44] Similarly, in the absence of the Cu segments, the interfacial coupling between Ni

and CoPt would promote a simultaneous switching of the magnetization in both magnetic segments. Hence, this configuration of the tri-segmented NWs provides access to various magnetization states depending on the relative orientation of the magnetization in each segment, as indicated in Figure 5b.
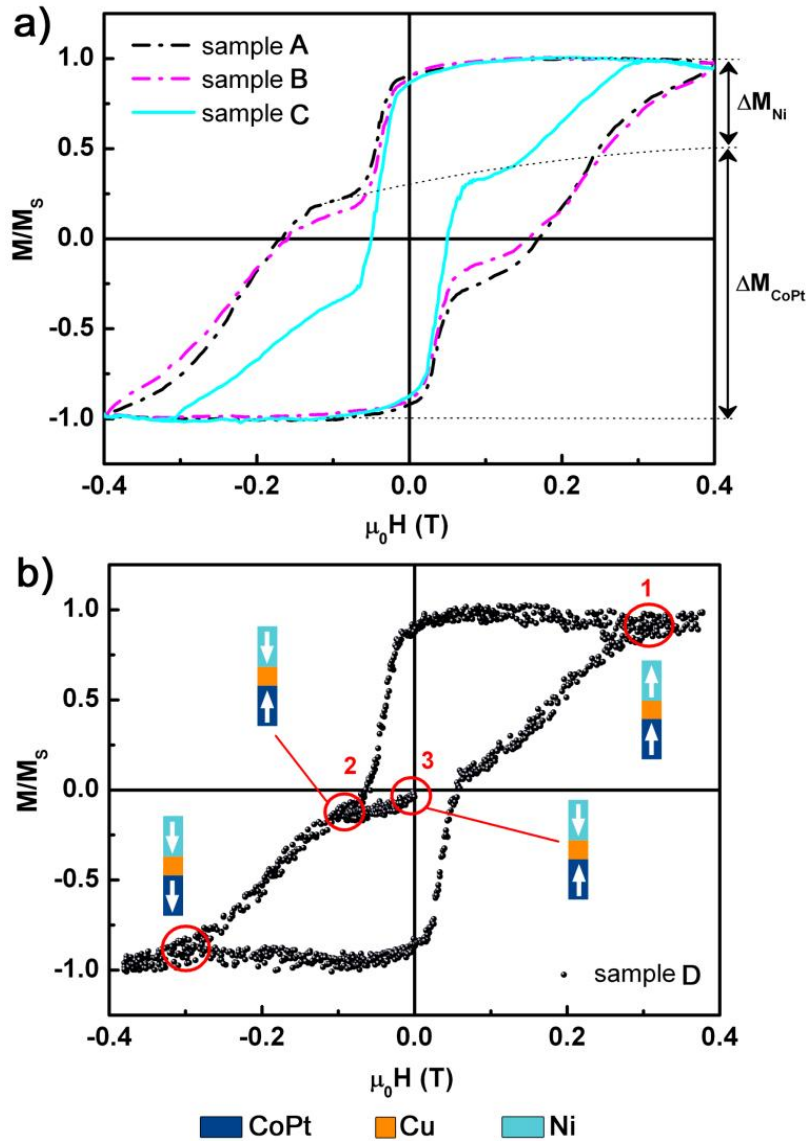

Figure 5. a) Staircase-shaped hysteresis loops corresponding to tri-segmented CoPt/Cu/Ni NWs with variable relative length ratios of the soft (Ni) and hard (CoPt) segments (samples A, B and

C; see Table 1). b) Hysteresis loop corresponding to an array of tri-segmented CoPt/Cu/Ni NWs (sample D) where the magnetization amplitudes of the Ni (ΔM_{Ni}) and CoPt (ΔM_{CoPt}) segments are virtually equal to each other. Indications in b) are the magnetic orientations of the two segments at different positions of the hysteresis loop.

Figure 5a reveals that while the contribution of Ni to the overall magnetization is larger than that of CoPt in sample C (in which the Ni segment is much longer than CoPt), the opposite is observed in samples A and B. Remarkably, the hysteresis loop shown in Figure 5b (sample D) exhibits virtually equal magnetization amplitudes from Ni and CoPt. Such precise tailoring of the hysteresis loop shape can be accomplished by varying the relative lengths of the Ni and CoPt segments (see Table 1). Since the saturation magnetization of Ni ($\mu_0 M_{S,Ni}$ = 0.6 T)[45] is approximately half that of CoPt ($\mu_0 M_{S,CoPt} \approx 1 - 1.3$ T)[46,47], the compensated situation (Figure 5b) occurs when the length of the Ni segment is approximately twice the length of CoPt (Table 1). In other words, in sample D (which is the one that corresponds to the EELS results shown in Figure 4) one has: $\mu_0 M_{S,Ni} * l_{Ni} * A \approx \mu_0 M_{S,CoPt} * l_{CoPt} * A$ (where, l designates "length" and A the cross-section area of the segments).

Sample	$\langle l_{CoPt}\rangle/\langle l_{Ni}\rangle$	$\Delta M_{CoPt} / \Delta M_{Ni}$	$M_{r,minor}/M_S$
A	~ 1.8	~ 3.2	0.31
B	~ 1.1	~ 2.2	0.23
C	~ 0.3	~ 0.6	-0.20
D	~ 0.5	~ 1.0	0

Table 1. Dependence of the relative magnetization amplitudes of the CoPt (ΔM_{CoPt}) and Ni (ΔM_{Ni}) segments, as well as the resulting remanent magnetization once the two segments are oriented antiparallel to each other (as depicted in Figure 5b, as a function of the average relative lengths of the CoPt (l_{CoPt}) and Ni (l_{Ni}) segments. Note that $M_{r,minor}$ is not the overall remanence magnetization of the whole hysteresis loops (which is close to 1 in all cases) but, instead, it denotes the remanent magnetization obtained when performing the minor loop sequence to set the antiparallel alignment between Ni and CoPt segments (i.e., when sweeping the field from positions 1 →2 →3 as indicated in Figure 5b. Samples A, B, C and D correspond to the ones whose hysteresis loops are shown in Figure 5.

3.4. Strategy to minimize interwire interactions

As mentioned in the Introduction, magnetic NWs are appealing for various technological applications (biomedical, catalytic, MEMS/NEMS, etc.) but the strength of interwire magnetic interactions, once the NWs are dispersed in a fluid, needs to be controlled and minimized in order to attain optimized performance. By taking advantage of the staircase shape of the hysteresis loops, it is possible to engineer a protocol to set an antiparallel alignment between the

soft and hard segments, and therefore reduce the overall remanent magnetization the NWs, when they are still embedded in the PC template. This can be done by first saturating the array of NWs using a strong positive magnetic field (position 1 in Figure 5b) and then applying a negative field sufficient to switch Ni to the negative orientation without reversing the magnetization of CoPt (position 2). Once the magnetic field is brought back to zero (position 3), the two segments remain antiparallel to each other and the resulting remanent magnetization ($M_{r,minor}$) will depend on the relative magnetization amplitudes of the Ni and CoPt segments (ΔM_{Ni} and ΔM_{CoPt}), i.e., on their length. The procedure is indicated in Figure 5b. Then, $M_{r,minor}/M_S$ can have either a positive value (samples A and B), negative value (sample C) or be virtually zero (sample D) (see Table 1). A comparative analytic calculation to show how the magnetic interaction energy outside the tri-segmented NW in sample D is reduced when the two segments are antiparallel to each other, with respect to the case of parallel alignment, is given in section 3.5. It is worth mentioning that such antiparallel alignment between the soft and hard segments will remain in the NWs dispersed in the fluid, provided that the applied external magnetic fields used to manipulate them do not exceed the coercivity of the soft segment. Fortunately, wireless manipulation of magnetic NWs in low Reynolds number aqueous environments is actually possible under the action of external fields of only a few tens of Oe, if combined with suitable magnetic field gradients.[46]
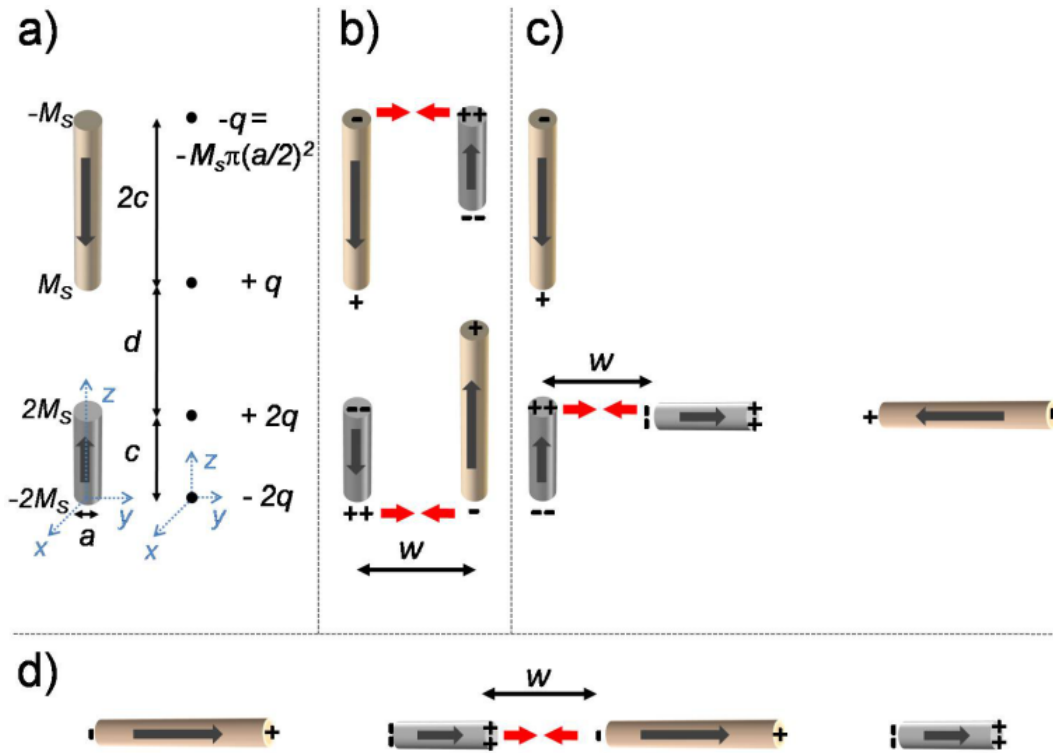
Figure 6. a) (Left) Schematic portrayal of a tri-segmented NW in antiferromagnetic (compensated) arrangement, where the hard segment (bottom) has length c and saturation magnetization $2\,M_S$ and the soft segment (top) has length c and saturation magnetization M_S. The non-magnetic segment is represented by the empty space of length d between the magnetic segments. The NW has diameter a. (Right) Simplified representation of the NW as a set of point magnetic charges. b-d) Different arrangements of NWs with attractive interactions (possibly leading to agglomeration) depending on the magnetization alignment between the magnetic segments. w is the distance between wires. The symbols + and - indicate the sign of the equivalent charges and the red arrows represent an attractive interaction between NWs.

3.5. Modeling the magnetic interaction energy between two tri-segmented NWs

For the sake of simplicity, we assume that each fully compensated tri-segmented NW has a circular cross-section of diameter a and it is composed of a hard segment of length c and uniform magnetization $2M_S$, a soft segment of length $2c$ and uniform magnetization M_S, and a non-magnetic segment represented by an empty space of length d between the two magnetic segments (left of Figure 6a). To some extent, this theoretical NW can be approximated as a set of pairs of point magnetic charges. That is, the hard segment is assumed equivalent to two charges of values $-2q$ and $2q$, where q would correspond to $M_S \pi a^2 / 4$, located at the center of the lower and upper surfaces of the segment, respectively. In the same way, the soft segment can be simplified as two charges of values q and $-q$ located at the center of the lower and upper surfaces, respectively (right of Figure 6a). The sign of each pair of charges changes depending on the orientation of the segment magnetization. To simulate the NWs of sample D the dimensions of the NWs are $a = c/10$ and $d = 2.5c$.

Once the NWs are properly magnetized (with the two segments aligned parallel or antiparallel) and dispersed in the fluid, they can be oriented in any direction. The relative orientation between two NWs can cause some attractive or repulsive movements between them because of the magnetic interaction that can result in the agglomeration of NWs. Figure 6 shows the possible ways of attractive interaction between NWs with antiparallel magnetic segments (Figure 6c) or parallel magnetic segments (Figures 6b and d). The symbols +, ++, - and --represent the equivalent charges $+q$, $+2q$, $-q$, and $-2q$, respectively, in the point charge approximation. In the case of antiparallel segments the NWs would be mainly attracted by forming a T-shape (Figure 6c) and in the parallel case the NWs attracted by following an antiferromagnetic coupling

(Figure 6b) or by aligning one along the other (Figure 6d). Other configurations of NWs interactions have weaker attractive interaction.

To analyze which NW configurations have lower magnetic attraction and, thus, weaker possibility of agglomeration, we plot in Figure 7 a comparison of the energies of the three different arrangements sketched in Figure 7. The magnetic interaction energy (normalized to $\mu_0 q^2/c$) of two NWs is plotted as a function of their distance w (normalized to c) when $d = 2.5c$. The results reveal that for interwire distances $w < c$ the interaction between T-shape NWs with antiparallel segments (solid black line) is lower than the one obtained in the case of antiferromagnetic coupled NWs with parallel segments (dashed red line). In these results the size of the non-magnetic segment is a relevant parameter because if $d < c$ the "T-shape" NWs configuration becomes the one with the largest interaction (not shown). Note that for interwire distances $w < 0.1c$ (that is $w < a$) the model of point charges is no longer valid. The inset of Figure 7 shows the case of large interwire distances, with the same interaction energies plotted in logarithmic scale (in absolute value). For comparison, the dependences $1/w^3$ (thin solid green line), that corresponds to a dipole-dipole magnetic interaction, and $1/w^5$ (thin dashed orange line), that corresponds to a quadrupole-quadrupole magnetic interaction are also plotted. These calculations reveal that for large interwire distances ($w > 50c$) the interaction between T-shape NWs is the lowest one and decays as $1/w^5$ (black line is parallel to the orange one), whereas for the configurations with parallel segment NWs, it decays as $1/w^3$ (red and blue lines are parallel to the green one).

The results of this section theoretically demonstrate that the agglomeration power between NWs with parallel magnetic segments is always larger than for NWs with antiparallel segments. Results do not qualitatively change when considering charged surfaces instead of point charges.
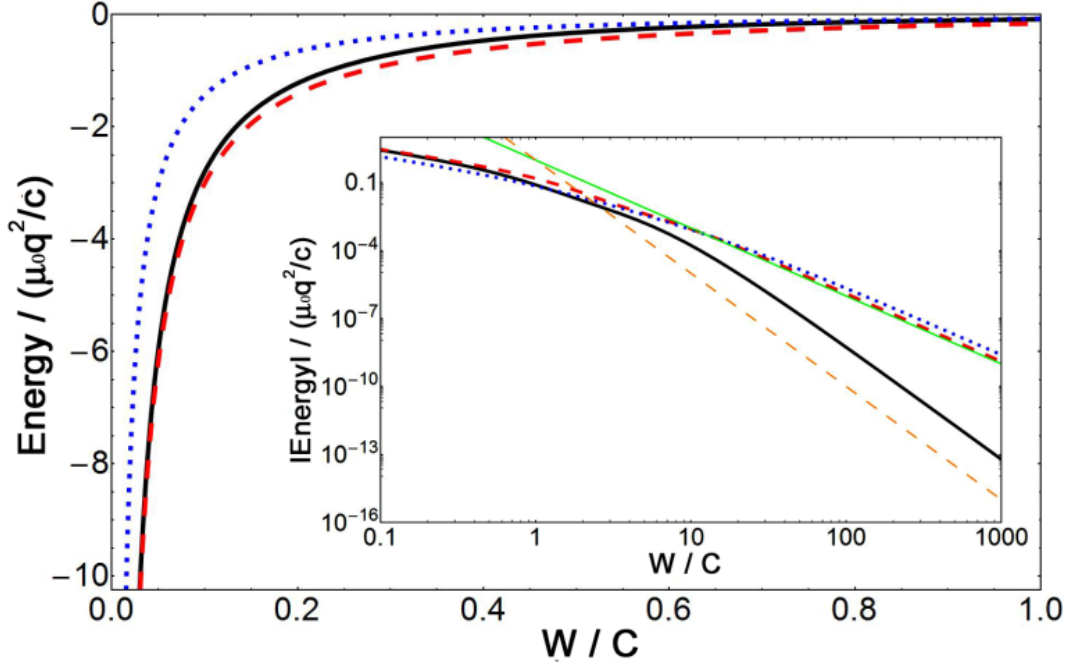
Figure 7. Interaction energy as a function of separation w between the NWs when $d = 2.5c$ for the different NW configurations of Figure 6: parallel magnetization alignment of Figure 6b (dashed red line), antiparallel alignment of Figure 6c (solid black line) and parallel alignment of Figure 6d (dotted blue line). The inset shows the absolute value of the energy of the main plot in a logarithmic scale. For comparison the dependences $1/w^3$ (thin solid green line) and $1/w^5$ (thin dashed orange line) are also plotted in the inset.

4. Conclusions

In summary, arrays of tri-segmented CoPt/Cu/Ni NWs with tunable segment lengths have been satisfactorily electrodeposited inside the pores of PC membranes and subsequently further structurally and magnetically characterized. These NWs exhibit staircase-like hysteresis loops, resulting from the two different coercivities of the soft (Ni) and hard ferromagnetic (CoPt)

segments. The magnetization amplitudes of the two ferromagnetic contributions depend on the relative lengths of CoPt and Ni. Antiparallel alignment between both ferromagnetic segments can be settled after positive saturation by applying a negative magnetic field sufficient to switch the Ni magnetization but smaller than the CoPt coercivity. In such antiparallel alignment, proper adjustment of the Ni and CoPt segment lengths eventually leads to virtually zero remanent magnetization (fully compensated NWs). The tri-segmented NWs can be then released from the PC membrane and satisfactorily dispersed in fluids. Analytical calculations are employed to corroborate that the magnetic interaction energy between two fully-compensated tri-segmented NWs (with two antiparallel magnetic segments with the same overall magnetic moment) is reduced with respect to a single NW with the same length or the tri-segmented NW with the two segments parallel to each other. Hence, this strategy is suitable to decrease the strength of magnetic interactions between NWs dispersed in liquids and is thus very appealing in all applications requiring the utilization of well-isolated magnetic single NWs, as well as to minimize NWs agglomeration during/after usage.

ASSOCIATED CONTENT

Supporting information.

Figure S1. SEM image of polycarbonate (PC) membrane with an average pore size of 50 nm.
Figure S2. SEM image of single-segmented Cu nanowires released from the PC membrane.

This material is available free of charge via the Internet at http://pubs.acs.org.

AUTHOR INFORMATION

Corresponding Author

* eva.pellicer@uab.cat

* jordi.sort@uab.cat

Author Contributions

The manuscript was written through contributions of all authors. All authors have given approval to the final version of the manuscript.

REFERENCES

(1) Brambilla, G.; Optical Fibre Nanowires and Microwires: A Review. *J. Opt.* **2010**, *12*, 043001–043020.

(2) O'Brien, L.; Petit, D.; Lewis, E. R.; Cowburn, R. P.; Read, D. E.; Sampaio, J.; Zeng, H. T.; Jausovec, A.-V. Tunable Remote Pinning of Domain Walls in Magnetic Nanowires. *Phys. Rev. Lett.* **2011**, *106*, 087204.

(3) Vázquez, M.; Vivas, L. G. Magnetization Reversal in Co-Base Nanowire Arrays. *Phys. Status. Solidi.* **2011**, *248*, 2368–2381.

(4) Sun, Y.; Zhang, F.; Xu, L.; Yin, Z.; Song, X. Roughness-Controlled Copper Nanowires and Cu nanowires–Ag Heterostructures: Synthesis and Their Enhanced Catalysis. *J. Mater. Chem. A* **2014**, *2*, 18583–18592.

(5) Espinosa, H. D.; Bernal, R. a; Minary-Jolandan, M. A Review of Mechanical and Electromechanical Properties of Piezoelectric Nanowires. *Adv. Mater.* **2012**, *24*, 4656–4675.

(6) Farhangfar, S. Size-Dependent Thermoelectricity in Nanowires. *J. Phys. D. Appl. Phys.* **2011**, *44*, 125403.

(7) Yogeswaran, U.; Chen, S. A Review on the Electrochemical Sensors and Biosensors Composed of Nanowires as Sensing Material. *Sensors* **2008**, *8*, 290–313.

(8) Zheng, G.; Patolsky, F.; Cui, Y.; Wang, W. U.; Lieber, C. M. Multiplexed Electrical Detection of Cancer Markers with Nanowire Sensor Arrays. *Nat. Biotechnol.* **2005**, *23*, 1294–1301.

(9) Fan, D. L.; Zhu, F. Q.; Cammarata, R. C.; Chien, C. L. Controllable High-Speed Rotation of Nanowires. *Phys. Rev. Lett.* **2005**, *94*, 247208.

(10) Kou, X.; Fan, X.; Dumas, R. K.; Lu, Q.; Zhang, Y.; Zhu, H.; Zhang, X.; Liu, K.; Xiao, J. Q. Memory Effect in Magnetic Nanowire Arrays. *Adv. Mater.* **2011**, *23*, 1393–1397.

(11) Parkin, S. S. P.; Hayashi, M.; Thomas, L. Magnetic Domain-Wall Racetrack Memory. *Science* **2008**, *320*, 190–194.

(12) Zhang, Z.; Dai, Y.; Yu, L.; Guo, M.; Huang, B.; Whangbo, M.-H. The Surface Termination Effect on the Quantum Confinement and Electron Affinities of 3C-SiC Quantum Dots: A First-Principles Study. *Nanoscale* **2012**, *4*, 1592–1597.

(13) Winkler, A.; Mühl, T.; Menzel, S.; Kozhuharova-Koseva, R.; Hampel, S.; Leonhardt, A.; Büchner, B. Magnetic Force Microscopy Sensors Using Iron-Filled Carbon Nanotubes. *J. Appl. Phys.* **2006**, *99*, 104905.

(14) Choi, D. S.; Park, J.; Kim, S.; Gracias, D. H.; Cho, M. K.; Kim, Y. K.; Fung, a.; Lee, S. E.; Chen, Y.; Khanal, S.; Baral, S.; Kim, J.-H. Hyperthermia with Magnetic Nanowires for Inactivating Living Cells. *J. Nanosci. Nanotechnol.* **2008**, *8*, 2323–2327.

(15) Prida, V. M.; García, J.; Iglesias, L.; Vega, V.; Görlitz, D.; Nielsch, K.; Barriga-Castro, E. D.; Mendoza-Reséndez, R.; Ponce, A.; Luna, C. Electroplating and Magnetostructural

Characterization of Multisegmented $Co_{54}Ni_{46}/Co_{85}Ni_{15}$ Nanowires from Single Electrochemical Bath in Anodic Alumina Templates. *Nanoscale Res. Lett.* **2013**, *8*, 263.

(16) Choi, J.; Oh, S. J.; Ju, H.; Cheon, J. Massive Fabrication of Free-Standing One-Dimensional Co/Pt Nanostructures and Modulation of Ferromagnetism via a Programmable Barcode Layer Effect. *Nano lett*. **2005**, *5*, 2179-2183.

(17) Bangar, M. A.; Hangarter, C. M.; Yoo, B.; Rheem, Y.; Chen, W.; Mulchandani, A.; Myung, N. V. Magnetically Assembled Multisegmented Nanowires and Their Applications. *Electroanalysis* **2009**, *21*, 61–67.

(18) Özkale, B.; Shamsudhin, N.; Chatzipirpiridis, G.; Hoop, M.; Gramm, F.; Chen, X.; Martí, X.; Sort, J.; Pellicer, E.; Pané, S. Multisegmented FeCo/Cu Nanowires: Electrosynthesis, Characterization, and Magnetic Control of Biomolecule Desorption. *ACS Appl. Mater. Interfaces* **2015**, *7*, 7389–7396.

(19) Zeeshan, M. A.; Pané, S.; Youn, S. K.; Pellicer, E.; Schuerle, S.; Sort, J.; Fusco, S.; Lindo, A. M.; Park, H. G.; Nelson, B. J. Graphite Coating of Iron Nanowires for Nanorobotic Applications: Synthesis, Characterization and Magnetic Wireless Manipulation. *Adv. Funct. Mater.* **2013**, *23*, 823–831.

(20) Piraux, L.; George, J.M.; Despres J. F.; Leroy C.; Ferain, E.; Legras, R.; Ounadjela, K.; Fert, A. Giant Magnetoresistance in Magnetic Multilayered Nanowires. *Appl. Phys. Lett*. **1994**, *65*, 2484-2486.

(21) Liu, K.; Nagodawithana, K.; Searson, P. C.; Chien, C. L. Perpendicular Giant Magnetoresistance of Multilayered Co/Cu nanowires. *Phys. Rev. B* **1995**, *51*, 7381-7384.

(22)   Doudin, B.; Redmond, G.; Gilbert, S. E.; Ansermet, J. –Ph. Magnetoresistance Governed by Fluctuations in Ultrasmall Ni/NiO/Co Junction. *Phys. Rev. Lett.* **1997**, *79*, 933-936.

(23)   Chong, Y. T.; Görlitz, D.; Martens, S.; Yau, M. Y. E.; Allende, S.; Bachmann, J.; Nielsch, K. Multilayered Core/Shell Nanowires Displaying Two Distince Magnetic Switching Events. *Adv. Mater*. **2010**, *22*, 2435-2439.

(24)   Piraux, L.; Renard, K.; Guillemet, R.; Mátéfi-Tempfli, S.; Mátéfi-Tempfli, M.; Antohe, V. A. Fusil, S.; Bouzehouane, K.; Cros, V. Template-Grown NiFe/Cu/NiFe Nanowires for Spin Transfer Devices. *Nano lett*. **2007**, *7*, 2563-2567.

(25)   Gapin, A. I.; Ye, X. R.; Chen, L. H.; Hong, D.; Jin, S. Patterned Media Based on Soft / Hard Composite Nanowire Array of Ni/CoPt. *IEEE Trans. Magn.* **2007**, *43*, 2151–2153.

(26)   Salabas, E. L.; Rumplecker, A.; Kleitz, F.; Radu, F. Schuth, F. Exchange Anisotropy in Nanocasted Co_3O_4 Nanowires. *Nano lett*. **2006**, *6*, 2977–2981.

(27)   Mourachkine, A.; Yazyev, O. V.; Ducati, C.; Ansermet, J. Template Nanowires for Spintronics Applications : Nanomagnet Microwave Resonators Functioning in Zero Applied. *Nano lett*. **2008**, *8*, 3683-3687.

(28)   Zhang, Y.; Ashall, B.; Doyle, G.; Zerulla, D.; Lee, G. U. Highly Ordered Fe−Au Heterostructured Nanorod Arrays and Their Exceptional Near-Infrared Plasmonic Signature. *Langmiur* **2012**, *28*, 17101-17107.

(29)   Su, Y.; Tang, J.; Yang, H.; Cheng, Z. Multifunctional Multisegmented $Co/CoPt_3$ Heterostructure Nanowires. *Nanoscale* **2013**, *5*, 9709-9713.

(30) Gao, W.; Manesh, K. M.; Hua, J.; Sattayasamitsathit, S.; Wang, J. Hybrid Nanomotor: A Catalytically/Magnetically Powered Adaptive Nanowire Swimmer. *Small* **2011**, *7*, 2047–2051.

(31) Alvarez-Lorenzo, C.; Concheiro, A. Smart Drug Delivery Systems: From Fundamentals to the Clinic. *Chem. Commun.* **2014**, *50*, 7743-7765.

(32) Reich, D. H.; Tanase, M.; Hultgren, A.; Bauer, L. A.; Chen, C. S.; Meyer, G. J. Biological Applications of Multifunctional Magnetic Nanowires (invited). *J. Appl. Phys.* **2003**, *93*, 7275-7280.

(33) Gao, F.; Gu, Z. Nano-Soldering of Magnetically Aligned Three-Dimensional Nanowire Networks. *Nanotechnology* **2010**, *21*, 115604.

(34) Kim, D.-H.; Rozhkova, E. A.; Ulasov, I. V.; Bader, S. D.; Rajh, T.; Lesniak, M. S.; Novosad, V. Biofunctionalized Magnetic-Vortex Microdiscs for Targeted Cancer-Cell Destruction. *Nat. Mater.* **2010**, *9*, 165–171.

(35) Chen, M.; Chien, C. L.; Searson P. C. Potential Modulated Multilayer Deposition of Multisegment Cu/Ni Nanowires with Tunable Magnetic Properties. *Chem. Mater*. **2006**, *18*, 1595-1601.

(36) Wong, J.; Greene, P.; Dumas, R. K.; Liu, K. Probing Magnetic Configurations in Co/Cu Multilayered Nanowires. *Appl. Phys. Lett*. **2009**, *94*, 032504.

(37) Sort, J.; Rodmacq, B.; Auffret, S.; Dieny, B. Pinned Synthetic Ferrimagnets with Perpendicular Anisotropy and Tuneable Exchange Bias. *Appl. Phys. Lett*. **2003**, *83*, 1800-1802.

(38) Baltz, V.; Rodmacq, B.; Bollero, A.; Ferré, J.; Landis, S.; Dieny, B. Balancing Interlayer Dipolar Interactions in Multilevel Patterned Media with out-of-Plane Magnetic Anisotropy. *Appl. Phys. Lett*. **2009**, *94*, 052503.

(39) Estradé, S.; Arbiol, J.; Peiró, F.; Abad, L.; Laukhin, V.; Balcells, L.; Martínez, B. Cationic Diffusion in $La_{2/3}Ca_{1/3}MnO_3$ Thin Films Grown on $LaAlO_3$ (001) Substrates. *Appl. Phys. Lett*. **2007**, *91*, 252503.

(40) López-Ortega, A.; Estrader, M.; Salazar-Alvarez, G.; Roca, A. G.; Nogués, J. Applications of Exchange Coupled Bi-Magnetic Hard/soft and Soft/hard Magnetic Core/shell Nanoparticles. *Phys. Rep.* **2015**, *553*, 1–32

(41) Yedra, L.; Xuriguera, E.; Estrader, M.; López-Ortega, A.; Baró, M. D.; Nogués, J.; Roldan, M.; Varela, M.; Estradé, S.; Peiró, F. Oxide Wizard: An EELS Application to Characterize the White Lines of Transition Metal Edges. *Microsc. Microanal*. **2014**, *20*, 698−705.

(42) Schönenberger, C. Template Synthesis of Nanowires in Porous Polycarbonate Membranes: Electrochemistry and Morphology. *J. Phys. Chem. B* **1997**, *5647*, 5497–5505.

(43) Jang, B.; Pellicer, E.; Guerrero, M.; Chen, X.; Choi, H.; Nelson, B. J.; Sort, J.; Pané, S. Fabrication of Segmented Au/Co/Au Nanowires: Insights in the Quality of Co/Au Junctions. *ACS Appl. Mater. Interfaces* **2014**, *6*, 14583-14589.

(44) Agramunt-Puig, S.; Del-Valle, N.; Pellicer, E.; Zhang, J.; Nogués, J.; Navau, C.; Sanchez, A.; Sort, J.; Modeling the Collective Magnetic Behavior of Highly-packed Arrays of Multi-segmented Nanowires. *New J. Phys.* **2016**, *18*, 013026.

(45) Ferré, R.; Ounadjela, K.; George, J. M.; Piraux, L.; Dubois, S. Magnetization Processes in Nickel and Cobalt Electrodeposited Nanowires. *Phys. Rev. B* **1997**, *56*, 14066–14075.

(46) Mitsuzuka, K.; Shimatsu, T.; Kikuchi, N.; Okamoto, S.; Aoi, H.; Kitakami, O. Remanence Coercivity of Dot Arrays of Hcp-CoPt Perpendicular Films. *J. Phys. Conf. Ser.* **2010**, *200*, 102005.

(47) Mallet, J.; Yu-Zhang, K.; Chien, C.-L.; Eagleton, T. S.; Searson, P. C. Fabrication and Magnetic Properties of Fcc $Co_X Pt_{1-X}$ Nanowires. *Appl. Phys. Lett*. **2004**, *84*, 3900-3902.

(48) Zhang, L.; Petit, T.; Lu, Y.; Kratochvil, B. E.; Peyer, K. E.; Pei, R.; Lou, J.; Nelson, B. J. Controlled Propulsion and Cargo Transport of Rotating Nickel Nanowires near a Patterned Solid Surface. *ACS Nano* **2010**, *4*, 6228–6234.

Table of Contents Graphic

released CoPt/Cu/Ni NWs

— CoPt segment   — Cu segment   — Ni segment